

Combined semiclassical and effective-mass Schrödinger approach for multiscale analysis of semiconductor nanostructures

Yang Xu and N. R. Aluru*

Beckman Institute for Advanced Science and Technology, University of Illinois at Urbana-Champaign, Urbana, Illinois 61801, USA

(Received 26 December 2006; published 3 August 2007)

A multiscale model, seamlessly combining semiclassical and quantum-mechanical theories, is proposed for electrostatic analysis of semiconductor nanostructures. A quantum potential criterion is used to determine if a local region in the semiconductor is semiclassical or quantum mechanical. If the local physical model is semiclassical, the charge density is directly computed by the semiclassical theory. If the local physical model is quantum mechanical, the charge density is calculated by using the theory of local density of states (LDOS). The LDOS is efficiently calculated from the Green's function by using Haydock's recursion method where the Green's function is expressed as a continued fraction based on the local effective-mass Schrödinger Hamiltonian. Once the charge density is determined, a Poisson equation is solved self-consistently to determine the electronic properties. The accuracy and efficiency of the multiscale method are demonstrated by considering examples from nanoelectromechanical systems (NEMS) and nanoelectronics. Furthermore, the regions where quantum-mechanical effects are significant are identified for the NEMS and nanoelectronic device structures.

DOI: [10.1103/PhysRevB.76.075304](https://doi.org/10.1103/PhysRevB.76.075304)

PACS number(s): 85.30.De, 85.85.+j, 85.35.-p, 41.20.Cv

I. INTRODUCTION

Semiconductor nanostructures, such as nanoelectromechanical systems (NEMS), semiconductor heterostructures, and nanoscale metal-insulator-semiconductor structures find applications in diverse areas such as communications, information technology, medical, mechanical, and aerospace technologies.¹⁻⁵ The design and characterization of semiconductor nanostructures can be accelerated by developing accurate and efficient physical models and computational design tools.²⁻⁸ Since the critical dimension of semiconductor nanostructures can vary from a few nanometers to several hundreds of nanometers, the use of an appropriate physical model to accurately and efficiently calculate the electronic properties is one of the central issues in electrostatic analysis of nanostructures.

Quantum-mechanical models are perhaps the most accurate theories available for electrostatic analysis of nanostructures. However, they are also the most expensive computational models. Semiclassical models can provide accurate results when carrier confinement is not significant. They are computationally less expensive compared to the quantum-mechanical models. Classical theory, based on the potential equation, is computationally the most attractive model, but it suffers from accuracy issues at the nanoscale. Typical semiconductor nanostructures contain regions where the semiclassical model is valid, as well as regions where quantum effects are important. If the semiclassical model is used for the entire device simulation, the electronic properties may not be accurately predicted where quantum effects are important. On the other hand, if quantum-mechanical models are used for the entire device, the extremely high computational cost limits the size of the device that can be simulated. To overcome these limitations, in the last few years several quantum correction based semiclassical approaches have been developed.⁹⁻¹⁴ While these methods approach the efficiency of the semiclassical approaches, they have some

drawbacks—for example, the self-consistent Coulomb potential obtained by these methods can deviate from the potential obtained from the quantum-mechanical models;^{14,15} the methods rely on fitting parameters and the solution can be sensitive to the fitting parameters used;^{10,11,14} in addition, the quantum corrected semiclassical models may not be accurate near heterojunctions and for devices involving tunneling.¹²⁻¹⁴ More recently, a parameter-free effective potential method has been developed,¹⁶ but this method is more expensive compared to the other effective potential methods. An attractive alternative to quantum correction based semiclassical approaches is to develop multiscale models where semiclassical theories are seamlessly combined with quantum-mechanical models for accurate and efficient analysis of semiconductor nanostructures.

In this paper, we propose a multiscale model for electrostatic analysis of semiconductor nanostructures. The multiscale scheme is conceptually illustrated in Fig. 1. The semiconductor device is first discretized into points, these points are referred to as the Poisson points. At each point, a quantum potential criterion, which will be discussed in detail later, is used to determine if the local region surrounding the point can be treated by a semiclassical or a quantum-mechanical model. If the quantum potential at a point is negligible compared to the Coulomb potential, the local physical model is semiclassical and the charge density is directly computed by the semiclassical approach,¹⁷ otherwise, the quantum-mechanical model is necessary to compute the charge density. When the quantum-mechanical model is required [in this paper, the quantum-mechanical effects are modeled by using the effective-mass Schrödinger (EMS) equation], one cannot directly solve the EMS equation in a local region to determine the charge distribution, as the boundary conditions on the wave functions are not known on the boundaries of the local region. Alternatively, in our multiscale model, the charge density is obtained from the local density of states (LDOS).¹⁷ To compute the LDOS, a sam-

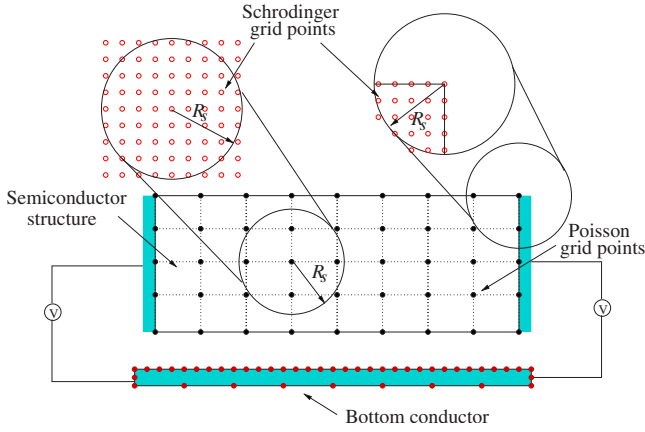


FIG. 1. (Color online) Illustration of the multiscale approach for a typical NEMS example consisting of a semiconductor beam structure and a bottom conductor. The semiconductor beam region is discretized into Poisson grid points. The closed circles represent the Poisson grid points and the total number of Poisson points is denoted by N_p . In the region where the quantum effects are important, a sampling region (typically circular, but other shapes can also be easily considered) is required to compute the LDOS at the Poisson point. The radius of the sampling region is denoted by R_S . To compute the LDOS of the sampling Poisson point, the sampling region is discretized using Schrödinger grid points. The open circles represent the Schrödinger points and the total number of Schrödinger points is denoted by N_S .

pling region (shown as a circular disk of radius R_S in Fig. 1) centered at the Poisson grid point is defined. The sampling region is discretized into Schrödinger grid points and the LDOS at the sampling Poisson point are calculated from the effective-mass Hamiltonian, which is constructed using the Schrödinger grid points in the sampling region. As shown in Fig. 1, if the sampling region intersects the physical boundaries of the semiconductor, then the sampling region is appropriately modified.

The multiscale method described above seamlessly combines the semiclassical and quantum-mechanical models. Quantum-mechanical effects are included only in the regions where they are necessary. As a result, semiconductor nanostructures which can be described entirely by semiclassical or quantum models or by combined semiclassical and quantum models are accurately modeled. The method is also efficient as quantum effects are included into the model by considering local sampling regions at each Poisson point instead of the entire nanostructure. The LDOS is computed from the Green's function of the effective-mass Hamiltonian matrix by using a recursion method. As the number of recursion levels computed is usually far less than the total number of Schrödinger points in the sampling region, the recursion method is an efficient approach to compute the LDOS. The rest of the paper is organized as follows. Section II describes the theory and implementation of the proposed multiscale model. Section III presents results for several examples demonstrating the accuracy and efficiency of the multiscale method and conclusions are given in Sec. IV.

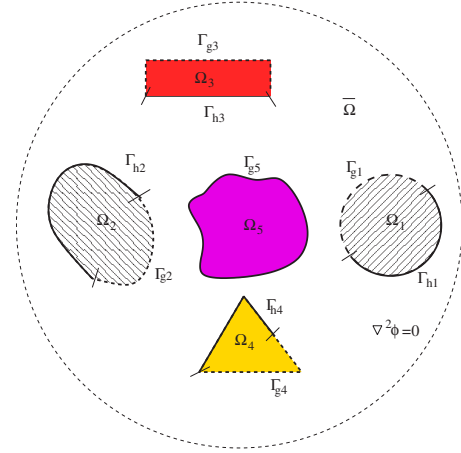


FIG. 2. (Color online) The electrostatic semiconductor system.

II. THEORY

A. Physical models

To illustrate the multiscale approach for electrostatic analysis of semiconductor nanostructures, we consider a general semiconductor system shown in Fig. 2. We deal with two-dimensional (2D) electrostatic problems in this paper, but the approach can be easily extended to three-dimensional problems. Consider a system of objects including semiconductors $(\Omega_1, \Omega_2, \dots, \Omega_{N_0})$, where N_0 is the number of objects, embedded in a uniform dielectric medium $\bar{\Omega}$ as shown in Fig. 2. Potential $\phi(\mathbf{x})$ and its normal derivative $q(\mathbf{x})$ are given by $g_\gamma(\mathbf{x})$ and $h_\gamma(\mathbf{x})$ on portions of the boundary of each semiconductor, $\Gamma_{g\gamma}$ and $\Gamma_{h\gamma}$, $\gamma=1, 2, \dots, N_0$, respectively, where $\mathbf{x}=(x, y)^T$ is the position vector of any point. The governing equations for electrostatic analysis along with the boundary conditions are given by¹⁷

$$\nabla[\epsilon_s \nabla \phi(\mathbf{x})] = -\rho(\mathbf{x}) = -e[p(\mathbf{x}) - n(\mathbf{x}) + N_D^+(\mathbf{x}) - N_A^-(\mathbf{x})] \quad \text{in } \Omega_\gamma, \quad \gamma = 1, \dots, N_0, \quad (1)$$

$$\nabla^2 \phi(\mathbf{x}) = 0 \quad \text{in } \bar{\Omega}, \quad (2)$$

$$\phi(\mathbf{x}) = g_\gamma(\mathbf{x}) \quad \text{on } \Gamma_{g\gamma}, \quad \gamma = 1, \dots, N_0, \quad (3)$$

$$q(\mathbf{x}) = \frac{\partial \phi(\mathbf{x})}{\partial \mathbf{n}} = h_\gamma(\mathbf{x}) \quad \text{on } \Gamma_{h\gamma}, \quad \gamma = 1, \dots, N_0, \quad (4)$$

where $\rho(\mathbf{x})$ is the charge density, $p(\mathbf{x})$ and $n(\mathbf{x})$ are hole and electron density, respectively, $N_D^+(\mathbf{x})$ and $N_A^-(\mathbf{x})$ are the ionized donor and acceptor concentrations, respectively, ϵ_s is the permittivity of the semiconductor material, and e is the elementary charge.

In the exterior domain $\bar{\Omega}$, the Laplace equation is satisfied as shown in Eq. (2). Note that the exterior domain $\bar{\Omega}$ is an open domain. A boundary integral formulation (BIE) of the 2D Laplace equation is used to treat the exterior electrostatic problem,¹⁸ i.e.,

$$\alpha(\mathbf{x})\phi(\mathbf{x}) = \sum_{\gamma=1}^{N_0} \int_{\Gamma_\gamma} \phi(\mathbf{x}') \frac{\partial G(\mathbf{x}, \mathbf{x}')}{\partial \mathbf{n}'} d\Gamma_\gamma(\mathbf{x}') - \sum_{\gamma=1}^{N_0} \int_{\Gamma_\gamma} \frac{\partial \phi(\mathbf{x}')}{\partial \mathbf{n}'} G(\mathbf{x}, \mathbf{x}') d\Gamma_\gamma(\mathbf{x}') + \phi_\infty, \quad (5)$$

$$\sum_{\gamma=1}^{N_0} \int_{\Gamma_\gamma} \frac{\partial \phi(\mathbf{x}')}{\partial \mathbf{n}'} d\Gamma_\gamma(\mathbf{x}') = 0, \quad (6)$$

where α is the corner tensor ($\alpha=1/2$ for smooth boundaries, see Ref. 19 for details) and $G(\mathbf{x}, \mathbf{x}') = \frac{1}{2\pi} \ln|\mathbf{x} - \mathbf{x}'|$ is the Green's function. In 2D problems, the potential at infinity is the reference potential, ϕ_∞ . The boundary integral equations, Eqs. (5) and (6), are coupled with the Poisson equation [Eq. (1)] through the interface conditions given by²⁰

$$\phi(\mathbf{x})|_{\text{BIE}} = \phi(\mathbf{x})|_{\text{Poisson}} \quad \text{on } \Gamma_{g\gamma}, \quad \gamma = 1, 2, \dots, N_0, \quad (7)$$

$$\epsilon_s \left. \frac{\partial \phi(\mathbf{x})}{\partial \mathbf{n}} \right|_{\text{Poisson}} + \epsilon_d \left. \frac{\partial \phi(\mathbf{x})}{\partial \mathbf{n}} \right|_{\text{BIE}} = \sigma_{\text{int}} \quad \text{on } \Gamma_{h\gamma}, \quad \gamma = 1, 2, \dots, N_0, \quad (8)$$

where $\phi(\mathbf{x})|_{\text{BIE}}$ and $\phi(\mathbf{x})|_{\text{Poisson}}$ are the potentials from the boundary integral equation and Poisson equation, respectively, $\left. \frac{\partial \phi(\mathbf{x})}{\partial \mathbf{n}} \right|_{\text{BIE}}$ and $\left. \frac{\partial \phi(\mathbf{x})}{\partial \mathbf{n}} \right|_{\text{Poisson}}$ are the normal derivatives of the potential from the boundary integral equation and Poisson equation, respectively, ϵ_d is the permittivity of the dielectric medium, and σ_{int} is the charge density on the exposed surface of the semiconductor. In this paper, for the purpose of illustrating the multiscale approach, the charge density on the surface is assumed to be zero. However, non-zero interface charge density σ_{int} can also be implemented easily. The potential $\phi(\mathbf{x})$ and the charge density $\rho(\mathbf{x})$ are obtained by solving Eqs. (1)–(8) self-consistently. In this paper, the interior Poisson's equation [Eq. (1)] is solved by using the finite difference method²¹ and the boundary integral equations [Eqs. (5) and (6)] are solved by the boundary element method.¹⁹

1. Semiclassical model: Semiclassical Poisson equation

When the geometrical characteristic length of the device is comparable to the Debye screening length,⁸ the semiclassical model is necessary to compute the charge density distribution. In the semiclassical model, the electron and hole density in Eq. (1) can be obtained as¹⁷

$$n(\mathbf{x}) = N_C \frac{2}{\sqrt{\pi}} \mathcal{F}_{1/2} \left(\frac{E_F - E_C(\mathbf{x})}{k_B T} \right), \quad (9)$$

$$p(\mathbf{x}) = N_V \frac{2}{\sqrt{\pi}} \mathcal{F}_{1/2} \left(\frac{E_V(\mathbf{x}) - E_F}{k_B T} \right), \quad (10)$$

where N_C and N_V are the effective density of states of conduction and valence band, respectively, $\mathcal{F}_{1/2}$ is the complete Fermi-Dirac integral of order 1/2, $E_C(\mathbf{x})$ is the conduction band energy given by $E_C(\mathbf{x}) = -e\phi(\mathbf{x}) + \frac{E_g}{2}$, where E_g is the

energy gap, $E_V(\mathbf{x})$ is the valence band energy given by $E_V(\mathbf{x}) = -e\phi(\mathbf{x}) - \frac{E_g}{2}$, E_F is the Fermi energy, k_B is the Boltzmann constant, and T is the temperature, which is set to be the room temperature in this work.

2. Quantum-mechanical model: Effective-mass Schrödinger equation

When the critical size of the device approaches the nanometer scale, quantum effects such as the carrier quantum confinement in the semiconductor structure become significant.⁸ The quantum effects in the device can be accounted for by solving the EMS equation in the entire semiconductor domain. The EMS equation is given by

$$H\psi_n(\mathbf{r}) = - \left[\frac{\hbar^2}{2} \frac{\partial}{\partial x} \left(\frac{1}{m_x^*} \frac{\partial}{\partial x} \right) + \frac{\hbar^2}{2} \frac{\partial}{\partial y} \left(\frac{1}{m_y^*} \frac{\partial}{\partial y} \right) \right] \psi_n(\mathbf{r}) + e\phi(\mathbf{r})\psi_n(\mathbf{r}) = E_n\psi_n(\mathbf{r}), \quad (11)$$

where H is the system Hamiltonian based on effective-mass approximation, \hbar is the reduced Planck's constant, m_x^* and m_y^* are the effective masses along the x and y axes, respectively, $\mathbf{r} = (x, y)^T$ is the position vector of any Schrödinger point, $\psi_n(\mathbf{r})$ is the n th eigenwave function, and E_n is the n th eigenvalue of the Hamiltonian H . If m_x^* and m_y^* are electron masses, then the Hamiltonian, $\psi_n(\mathbf{r})$, and E_n are computed for electrons. If m_x^* and m_y^* are hole masses, then the Hamiltonian, $\psi_n(\mathbf{r})$, and E_n are for holes. After solving the eigen system, all the eigen energies and eigen wave functions are known. Then the electron density $n(\mathbf{r})$ and hole density $p(\mathbf{r})$ in Eq. (1) can be computed by

$$n(\mathbf{r}) = N_n \sum_n |\psi_n(\mathbf{r})|^2 \mathcal{F}_{-1/2} \left(\frac{E_F - E_n}{k_B T} \right), \quad (12)$$

$$p(\mathbf{r}) = N_p \sum_n |\psi_n(\mathbf{r})|^2 \mathcal{F}_{-1/2} \left(\frac{E_n - E_F}{k_B T} \right), \quad (13)$$

where the coefficients N_n and N_p are

$$N_n = g_n \frac{1}{\pi} \left(\frac{2m_n^* k_B T}{\hbar^2} \right)^{1/2}, \quad (14)$$

$$N_p = g_p \frac{1}{\pi} \left(\frac{2m_p^* k_B T}{\hbar^2} \right)^{1/2} \quad (15)$$

for the conduction band and valence band, respectively, $\mathcal{F}_{-1/2}$ is the complete Fermi-Dirac integral of order $-1/2$, constants g_n and g_p are the semiconductor conduction band degeneracy and valence band degeneracy, respectively, m_n^* and m_p^* are the density of state masses of electrons and holes, respectively, and the summations in Eqs. (12) and (13) are over all the energy levels. Note that the solution of the EMS equation [Eq. (11)] requires an eigensolution in the entire semiconductor domain. This can be expensive and inefficient when simulating large devices.

B. Multiscale approach

Typical semiconductor nanostructures contain regions where the semiclassical models are valid, but they also contain regions where quantum effects are important. If a semiclassical model is used for the entire device, the electronic properties may not be predicted accurately in the region where quantum effects are important. On the other hand, if quantum-mechanical models are used for the entire device, the extremely high computational cost limits the size of the device that can be simulated. Multiscale models, which seamlessly combine the semiclassical and quantum models, can be accurate and efficient to predict the electronic properties of semiconductor nanostructures. The use of direct domain decomposition, where the EMS model and the semiclassical model are employed in different regions and combined through interface boundary conditions, can be hard to implement as the wave functions are nonlocal and imposition of a wave function as a boundary condition between the semiclassical and quantum regions can be difficult.

To overcome this difficulty, we develop a multiscale model which seamlessly combines quantum-mechanical and semiclassical models. In the region or at the Poisson grid points where the semiclassical model is not valid, the Poisson grid point is represented by a fine-scale model or the quantum model (see Fig. 1). A Hamiltonian is first constructed by using the fine-scale grid points or the Schrödinger grid points. Using the Hamiltonian, the elements of the Green's function (GF) matrix are then computed by²²

$$\begin{aligned} \lim_{\eta \rightarrow 0^+} G_{j,j'}(E + i\eta) &= \lim_{\eta \rightarrow 0^+} \{[(E + i\eta)\mathbf{I} - H]^{-1}\}_{j,j'} \\ &= \lim_{\eta \rightarrow 0^+} \sum_n \frac{\psi_n(\mathbf{r}_j) \psi_n^*(\mathbf{r}_{j'})}{E - E_n + i\eta}, \\ j, j' &= 1, 2, \dots, N_S, \end{aligned} \quad (16)$$

where \mathbf{I} is the identity matrix, $G_{j,j'}$ denotes the j th row and j' th column entry of the Green's function matrix G , E is the energy, and $\psi_n^*(\mathbf{r}_{j'})$ is the conjugate value of $\psi_n(\mathbf{r}_{j'})$. By using the identity for the δ function given by

$$\delta(E - E_n) = -\frac{1}{\pi} \lim_{\eta \rightarrow 0^+} \text{Im} \frac{1}{E - E_n + i\eta}, \quad (17)$$

the diagonal entries of the GF matrix can be written as

$$\lim_{\eta \rightarrow 0^+} \text{Im} G_{j,j}(E + i\eta) = -\pi \sum_n \delta(E - E_n) |\psi_n(\mathbf{r}_j)|^2. \quad (18)$$

Using the definition of the LDOS,²²

$$N(\mathbf{r}_j, E) = \sum_n \delta(E - E_n) |\psi_n(\mathbf{r}_j)|^2, \quad (19)$$

and comparing Eq. (19) with Eq. (18), the LDOS at the Schrödinger point \mathbf{r}_j , denoted by $N(\mathbf{r}_j, E)$, can be expressed as the imaginary part of the diagonal elements of the GF matrix (see, e.g., Ref. 22 for details),

$$N(\mathbf{r}_j, E) = -\pi^{-1} \lim_{\eta \rightarrow 0^+} \text{Im} G_{j,j}(E + i\eta). \quad (20)$$

If the Hamiltonian of electrons is used in Eq. (16), then the LDOS [$N(\mathbf{r}, E)$] computed in Eq. (20) is that of the electrons [denoted by $N_e(\mathbf{r}, E)$] and if the Hamiltonian of holes is used in Eq. (16), then the hole LDOS [denoted by $N_h(\mathbf{r}, E)$] are computed. After $N_e(\mathbf{r}, E)$ and $N_h(\mathbf{r}, E)$ are known, the electron density $n(\mathbf{r})$ and the hole density $p(\mathbf{r})$ can be obtained by

$$n(\mathbf{r}) = \int_{E_C(\mathbf{r})}^{\infty} N_e(\mathbf{r}, E) f_e(E) dE, \quad (21)$$

$$p(\mathbf{r}) = \int_{-\infty}^{E_V(\mathbf{r})} N_h(\mathbf{r}, E) f_h(E) dE, \quad (22)$$

where $f_e(E)$ is the Fermi-Dirac distribution for electrons given by

$$f_e(E) = \frac{1}{1 + e^{(E - E_F)/k_B T}}, \quad (23)$$

and $f_h(E)$ is the Fermi-Dirac distribution for holes given by

$$f_h(E) = \frac{1}{1 + e^{(E_F - E)/k_B T}}. \quad (24)$$

Comparing Eqs. (21) and (22) with Eqs. (12) and (13), we note that the wave functions are not required explicitly in the LDOS approach to compute the electron and hole density. In addition, for each sampling region, we only need to compute the LDOS at the Poisson point (or the corresponding Schrödinger point), where the sampling region is centered.

In summary, in the multiscale model described above, instead of directly coupling the semiclassical and quantum-mechanical regions, in the regions where semiclassical theory is not valid, the electron and hole density are computed by using the LDOS method. This approach enables seamless coupling of quantum-mechanical theory into the semiclassical theory.

1. Efficient calculation of LDOS

To compute the LDOS by using Eq. (20), only the diagonal entries of the GF matrix are needed. The direct matrix inversion in Eq. (16) to compute the diagonal entries of $G(E)$ is numerically expensive. As an alternative method, if the Hamiltonian matrix can be transformed into a tridiagonal form, then the diagonal entries of the GF matrix can be easily obtained. Since the effective-mass Hamiltonian matrix is symmetric, we can write the tridiagonalized Hamiltonian H^{TD} as

$$H^{TD} = \begin{bmatrix} a_1 & b_2 & & & & \\ b_2 & a_2 & b_3 & & & \\ & \ddots & \ddots & \ddots & & \\ & & b_{N_S-1} & a_{N_S-1} & b_{N_S} & \\ & & & b_{N_S} & a_{N_S} & \end{bmatrix}, \quad (25)$$

where N_S is the total number of Schrödinger points used to construct the Hamiltonian, and the modified GF matrix $\tilde{G}(z)$ using H^{TD} is given by

$$\tilde{G}(z) = (z\mathbf{I} - H^{TD})^{-1}, \quad (26)$$

where $z = E + i\eta$. Denoting L to be the orthogonal transformation matrix used to construct H^{TD} , the relation between $G(z)$ and $\tilde{G}(z)$ is given by

$$\tilde{G}(z) = LG(z)L^T. \quad (27)$$

By using the symmetric and tridiagonal properties of H^{TD} , the entries of $\tilde{G}(z)$ can be represented as a continued fraction.²³ For example, the first diagonal entry of $\tilde{G}(z)$ is given by

$$\tilde{G}_{1,1}(z) = \frac{1}{z - a_1 - \frac{b_2^2}{z - a_2 - \frac{b_3^2}{\ddots \frac{b_{N_S}^2}{z - a_{N_S}}}}} \quad (28)$$

where $a_k, k=1, \dots, N_S$, and $b_k, k=2, \dots, N_S$, are the recursion coefficients (RCs).

The calculation of all the diagonal and the off-diagonal elements of the tridiagonalized H^{TD} can still be expensive.²⁴ Since the contribution of successive RCs to the LDOS decreases significantly and the exact coefficients can be replaced by constant values after a certain number of levels without reducing the accuracy significantly,²⁵ we can compute the first N_L -level coefficients (N_L being far less than N_S) accurately and approximate all the high-order coefficients by a_{N_L} and b_{N_L} . That is, the continued fraction in Eq. (28) is calculated exactly up to N_L levels and the rest of the continued fraction is approximated by a terminator, which represents an infinite level continued fraction.²⁵ Therefore $\tilde{G}_{1,1}(z)$ can be rewritten as

$$\tilde{G}_{1,1}(z) = \frac{1}{z - a_1 - \frac{b_2^2}{z - a_2 - \frac{b_3^2}{\ddots \frac{b_{N_L-1}^2}{z - a_{N_L-1} - b_{N_L}^2 t(z)}}}} \quad (29)$$

where $t(z)$ is defined as the square root terminator (SRT) function and is given by

TABLE I. Calculation of LDOS by the Lanczos algorithm.

Algorithm 1
1. Construct the entries of the local Hamiltonian H in the i th sampling region (the coordinate of the Poisson point is denoted as \mathbf{x}_i).
2. Choose an initial state ξ_1 as defined in Eq. (31).
3. Calculate $a_1 = \xi_1^T H \xi_1$.
4. Calculate a_{k+1}, b_{k+1} , and ξ_{k+1} , $k=1, \dots, N_L-1$, using Eq. (32).
5. Use a_{N_L}, b_{N_L} to compute the square root terminator, $t(z)$, by Eq. (30).
6. Calculate $\tilde{G}_{1,1}(z)$ using Eq. (29), and the diagonal element of the Green's function matrix at the point of interest \mathbf{r}_j , $G_{j,j}(z)$, is obtained through Eq. (33) where $\mathbf{r}_j = \mathbf{x}_i$.
7. Compute the LDOS at $\mathbf{r}_j (= \mathbf{x}_i)$ through Eq. (20).

$$t(z) = \frac{1}{b_{N_L}} \left[\left(\frac{z - a_{N_L}}{2b_{N_L}} \right) - i \sqrt{1 - \left(\frac{z - a_{N_L}}{2b_{N_L}} \right)^2} \right]. \quad (30)$$

The tridiagonalization of the Hamiltonian matrix can be realized by using the Lanczos algorithm.²³ In the numerical scheme, for a given position index j (i.e., to compute $G_{j,j}$ corresponding to the Schrödinger grid point r_j), the starting Lanczos state is set as

$$\xi_1 = (\dots, 0, 1, 0, \dots)^T, \quad (31)$$

where the only nonzero entry is located in the j th position. We also set $b_1=0$, $\xi_0=0$, and we can compute a_1 as $a_1 = \xi_1^T H \xi_1$. The Lanczos recursion relation for the Hamiltonian matrix H applied to a sequence of vectors,

$$\tilde{\xi}_{k+1} = (H - a_k \mathbf{I}) \xi_k - b_k \xi_{k-1}, \quad k=1, 2, \dots, N_L-1, \quad (32)$$

generates the RCs, $a_{k+1} = \tilde{\xi}_{k+1}^T H \tilde{\xi}_{k+1}$, $b_{k+1} = \sqrt{\tilde{\xi}_{k+1}^T \tilde{\xi}_{k+1}}$, and the set of normalized vectors, $\xi_{k+1} = \tilde{\xi}_{k+1} / b_{k+1}$, $k=1, 2, \dots, N_L-1$. Once a_{N_L} and b_{N_L} are known, the SRT function, $t(z)$, is then computed. After that, the first diagonal entry of the modified GF matrix, $\tilde{G}_{1,1}(z)$, can be calculated by Eq. (29). From the Lanczos algorithm, the orthogonal transformation matrix, L , is computed as $L = [\xi_1 \xi_2 \dots \xi_k \dots]$. Because there is only one nonzero entry for ξ_1 , it is easy to show that

$$G_{j,j}(z) = \tilde{G}_{1,1}(z). \quad (33)$$

Since only the first N_L recursion levels are calculated and N_L is usually far less than N_S , the recursion technique is an efficient approach to compute the LDOS. The calculation of LDOS by the Lanczos algorithm is summarized in algorithm 1, see Table I.

2. Criterion for physical models

Quantum-mechanical laws come into action when the carriers are confined in a region with characteristic size of the order of several nanometers.²⁶ There are several criteria to determine whether the local region is quantum mechanical or semiclassical. For example, a straightforward way is to cal-

culate the carrier density by the quantum model at the Poisson point, and to compare the carrier density with that from the semiclassical model. If the difference between the two is smaller than a given tolerance, then we can treat the Poisson point in a semiclassical way, otherwise, the point is quantum mechanical. This criterion can, however, be expensive as we need to compute the LDOS at every Poisson point using the quantum model. Other criterion such as the method proposed in Ref. 16 can also be used. Alternatively, a relatively cheap criterion, which is referred to as the quantum potential criterion, is used in this paper. The quantum potential $\phi_q(\mathbf{x})$ can be used to determine whether the quantum effects are important locally or can be neglected.¹¹ When the electrons are the major carriers in the device, the quantum potential is given by

$$\phi_q(\mathbf{x}) = -\frac{\hbar^2}{8} \left[\frac{\partial}{\partial x} \left(\frac{1}{m_x^*} \frac{\partial \ln n(\mathbf{x})}{\partial x} \right) + \frac{\partial}{\partial y} \left(\frac{1}{m_y^*} \frac{\partial \ln n(\mathbf{x})}{\partial y} \right) \right]. \quad (34)$$

When the holes are the major carriers in the device, $n(\mathbf{x})$ is replaced by $p(\mathbf{x})$, and the electron effective masses are replaced by the hole effective masses. To determine whether the sampling Poisson point is semiclassical or quantum mechanical, we first calculate the quantum potential by Eq. (34). By comparing the quantum potential $\phi_q(\mathbf{x})$ with the Coulomb potential $\phi(\mathbf{x})$, the semiclassical model is used at the sampling Poisson point if $|\phi_q(\mathbf{x})|/\max|\phi(\mathbf{x})| \leq \nu_{\text{tol}}$, where ν_{tol} is the given tolerance, otherwise, the quantum-mechanical model is used at the sampling Poisson point.

3. Size of the sampling region

According to the ‘‘nearsightedness’’ principle,²⁷ the local electronic properties, such as the local charge density, depend significantly on the effective external potential in only the nearby region. The changes of that potential, no matter how large, beyond a distance R_S , have a limited effect on the local electronic properties, which rapidly decay to zero as a function of R_S .²⁸ In this paper, we use the ‘‘nearsightedness’’ principle to determine the size of the sampling region. Kohn²⁸ gave an approximate expression for the nearsightedness radius $R(r_0, \Delta n)$ centered at r_0 for a semiconductor as

$$R(r_0, \Delta n) \approx \frac{1}{2q_{\text{eff}}} \ln \frac{\tilde{n}}{\Delta n}, \quad (35)$$

where q_{eff} is the decay constant of the density matrix given by $q_{\text{eff}} = \frac{1}{2} \sqrt{E_g m^* / \hbar^2}$, m^* is the effective mass of electrons and holes, \tilde{n} is the local charge density which can be approximated by the equilibrium charge density at r_0 , $\rho(r_0)$, and Δn is the finite maximum asymptotic charge density due to any perturbation outside of the circle of radius R . $R(r_0, \Delta n)$ defines the radius where the change in density at r_0 as a result of any perturbation outside of R does not exceed Δn . For example, from Eq. (35), if we require the relative density error to satisfy the condition $\frac{\Delta n}{\tilde{n}} < 5 \times 10^{-3}$, we obtain the nearsightedness radius for silicon to be approximately 6 nm. In this paper, we choose the radius of sampling region R_S equal to the nearsightedness radius for simplicity.

C. Algorithm for the self-consistent multiscale model

Algorithm 2 summarizes the procedure for self-consistent electrostatic analysis of semiconductor nanostructures by using the combined semiclassical and EMS multiscale approach (see Table II).

III. RESULTS

A. 2D fixed-fixed beam case

To illustrate the multiscale model, we first choose a 2D fixed-fixed beam as shown in Fig. 3. The N -doped (10^{18} cm^{-3}) silicon beam is clamped above a ground plane and a voltage, V_{app} , is applied between the ground plane and the beam. The Schottky contact effect is ignored in this case for simplicity. The width of the silicon beam is $W=20$ nm, length is $L=40$ nm, and the gap is $G=20$ nm. We assume that the beam and the bottom conductor are infinitely long along the z axis (z axis is pointing out of the paper). To solve the Poisson and EMS equations, we first use the Poisson and Schrödinger grids to discretize the domain. The Poisson grid spacings along the x and y axes are denoted by Δx_P and Δy_P , respectively. The Schrödinger grid spacings along the x and y axes are denoted by Δx_S and Δy_S , respectively. For simplicity, we use a square grid for both the Poisson and the Schrödinger domains, i.e., $\Delta x_P = \Delta y_P$, $\Delta x_S = \Delta y_S$.

To understand how the various parameters in the multiscale model effect the accuracy, efficiency, and the convergence rate of the method, we first study the effect of the radius of the sampling region R_S on the convergence rate. Figure 4 shows the error as a function of R_S , when R_S is varied from 2 to 12 nm, with fixed grid spacings $\Delta x_P (= \Delta y_P) = 0.8$ nm and $\Delta x_S (= \Delta y_S) = 0.4$ nm. From Fig. 4, we observe that the error decays as R_S is increased. When R_S is equal to 6 nm, the error between the multiscale model and the EMS model is less than 2%.

Next we test the influence of the number of recursion levels N_L on the convergence rate for a given $R_S = 6$ nm and $\Delta x_P = \Delta y_P = 2\Delta x_S = 2\Delta y_S = 0.8$ nm. Figure 5 shows the error as a function of N_L , when N_L is varied from 10 to 40 levels. From Fig. 5, we notice that the error decays quickly as N_L increases. When N_L is 30, the error between the multiscale model and the EMS model is less than 2%.

For the silicon beam shown in Fig. 3, the applied electric field and the physical boundaries form the quantum wells which confine the electrons and quantize the energy levels. When the confinement and quantization are strong, they will

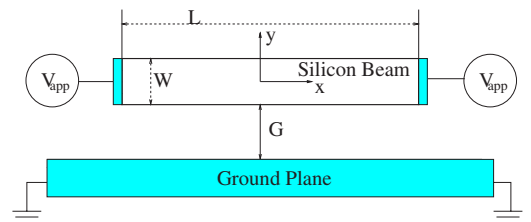


FIG. 3. (Color online) A typical nanoswitch consisting of a fixed-fixed semiconductor and a bottom conductor, where $L=2W=40$ nm, $G=20$ nm with an applied voltage $V_{\text{app}}=-2.0$ V.

TABLE II. A complete algorithm for self-consistent multiscale electrostatic analysis of semiconductor nanostructures.

Algorithm 2

1. Discretize the domain of the semiconductor beam into N_p Poisson grid points for solving the Poisson equation and discretize the boundary of the semiconductors and conductors (if any) into BIE grid points for solving the BIE equation (see Fig. 1 for an example).
2. Set $k=0$, solve the semiclassical Poisson model [Eqs. (1) and (5)–(10)] and obtain the potential distribution $\phi^{(0)}$, electron density $n^{(0)}$, and hole density $p^{(0)}$.
3. **Repeat**
4. **for** each Poisson grid point, $i=1$ to N_p **do**
5. compute the quantum potential $\phi_q(\mathbf{x}_i)$ using Eq. (34) and choose the appropriate physical model to be used at this Poisson grid point
6. **if** the physical model is *semiclassical* **then**
7. compute the charge density $n_i^{(k+1)}$ and $p_i^{(k+1)}$ using Eqs. (9) and (10)
8. **else if** the physical model is *quantum mechanical* **then**
9. define the local sampling region by Eq. (35) according to the accuracy level, and discretize the local sampling region into Schrödinger grid points
10. construct the entries of the local Hamiltonian matrix by using $\phi^{(k)}$
11. use the recursion technique given in Algorithm 1 to compute the LDOS
12. compute $n_i^{(k+1)}$ and $p_i^{(k+1)}$ at the Schrödinger point ($\mathbf{r}_j=\mathbf{x}_j$) using Eqs. (21) and (22)
13. **end if**
14. **end for**
15. solve the coupled BIE/Poisson equations [Eqs. (1) and (5)–(8)] to update the potential distribution $\phi^{(k+1)}$
16. **if** $\max|n_i^{(k+1)}-n_i^{(k)}| < \theta_{\text{tol}}^n$, $\max|p_i^{(k+1)}-p_i^{(k)}| < \theta_{\text{tol}}^p$, and $\max|\phi_i^{(k+1)}-\phi_i^{(k)}| < \theta_{\text{tol}}^\phi$, where θ_{tol}^n and θ_{tol}^ϕ are the error tolerances for the charge density and potential, respectively, **then**
17. stop and go to step 22
18. **else**
19. $k=k+1$
20. **end if**
21. **until** a self-consistent solution is obtained.
22. Output the results.

change the electron density distribution significantly. Since the quantum potential [Eq. (34)] is the Laplacian of the logarithm of the electron density distribution, when it becomes nontrivial compared to the Coulomb potential, it can be used

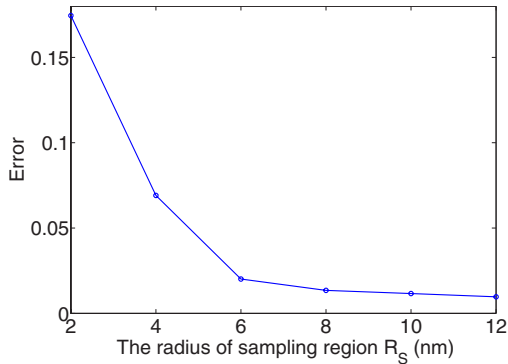


FIG. 4. (Color online) Comparison of error between the multiscale approach and the EMS model as a function of R_S . Error is defined as $\text{error} = 1 / (|\rho_{\text{max}}^{\text{ref}}| \sqrt{1 / N_p \sum_{i=1}^{N_p} [\rho^{\text{ref}}(\mathbf{x}_i) - \rho^a(\mathbf{x}_i)]^2})$, where ρ^{ref} and ρ^a are the reference EMS solution and the multiscale solution, respectively, obtained by using $\Delta x_p = \Delta y_p = 2\Delta x_s = 2\Delta y_s = 0.8$ nm.

to identify the quantum region. With R_S and N_L chosen to be 6 nm and 30 levels, respectively, Fig. 6 shows the multiscale domain of the silicon beam obtained by using the quantum

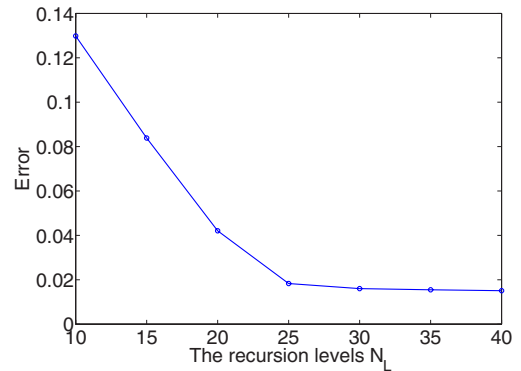


FIG. 5. (Color online) Comparison of error between the multiscale approach and the EMS model as a function of N_L . Error is defined as $\text{error} = 1 / (|\rho_{\text{max}}^{\text{ref}}| \sqrt{1 / N_p \sum_{i=1}^{N_p} [\rho^{\text{ref}}(\mathbf{x}_i) - \rho^a(\mathbf{x}_i)]^2})$, where ρ^{ref} and ρ^a are the reference EMS solution and the multiscale solution, respectively, obtained by using $\Delta x_p = \Delta y_p = 2\Delta x_s = 2\Delta y_s = 0.8$ nm. In the multiscale solution, the sampling radius R_S is set equal to 6 nm.

potential criterion. The shaded region indicates the quantum region, whereas the white region indicates the semiclassical region. Since we know that the electric field penetrates deeper into the middle-bottom region than the side regions, the characteristic length of the quantum region in the middle-bottom of the beam is larger than that in the sides, as shown in Fig. 6.

A comparison of the detailed solutions for the electron density and the potential obtained by the semiclassical, EMS, and the multiscale method are presented in Fig. 7. Figures 7(a) and 7(b) show the potential and the electron density, respectively, in the fixed-fixed silicon beam obtained by the multiscale method. In Figs. 7(c) and 7(e), the potential distributions along the y axis for the $x=0$ cross section and along the x axis for the $y=0$ cross section obtained with the semiclassical, EMS, and the multiscale models are compared. In Figs. 7(d) and 7(f), the electron distributions along the y axis for the $x=0$ cross section and along the x axis for the $y=0$ cross section obtained with the three methods are compared. From the above comparison, the electron density obtained with the semiclassical method close to the boundary is much larger than that of the multiscale method as it does not consider the quantum confinement effects. The higher electron density close to the boundary obtained by the semiclassical method results in a different potential distribution compared to the multiscale method. From these results, we observe that the semiclassical model fails to predict the electronic properties, whereas the results from the multiscale model are identical to the results from the EMS model. For this example, the multiscale method is found to be about 60 times faster compared to directly solving the EMS model.

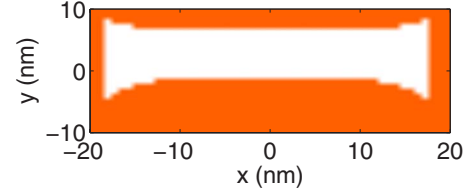


FIG. 6. (Color online) Illustration of the multiscale domain for the fixed-fixed silicon beam with dimensions of $L=2W=40$ nm, $G=20$ nm. The semiclassical model is applicable at the sampling Poisson point if $|\phi_q(\mathbf{x})|/\max|\phi| \leq \nu_{\text{tol}}$, where ν_{tol} is the given tolerance (a value of 1×10^{-2} is used here). The shaded region indicates the quantum region, whereas the white region indicates the semiclassical region.

B. Capacitance of a simple NEMS system

In the second example, shown in Fig. 8, we compute the capacitance of two semiconductors. Both the silicon beams have the same size, where the width of a beam is denoted by W , the length is L , and the gap between them is G . The upper beam and the lower beam are doped N -type ($N_D = 10^{17} \text{ cm}^{-3}$) and P -type ($N_A = 10^{17} \text{ cm}^{-3}$), respectively. The Schottky contact effect is also ignored in this example. The capacitance of this system is given by the general relation

$$\begin{bmatrix} dQ_1 \\ dQ_2 \end{bmatrix} = \begin{bmatrix} C_{11} & C_{12} \\ C_{21} & C_{22} \end{bmatrix} \begin{bmatrix} dV_1 \\ dV_2 \end{bmatrix}, \quad (36)$$

where C_{11} and C_{22} denote the self-capacitances of semiconductors 1 and 2, respectively, C_{21} and C_{12} are the mutual capacitances, Q_1 and Q_2 are the charges on semiconductors 1

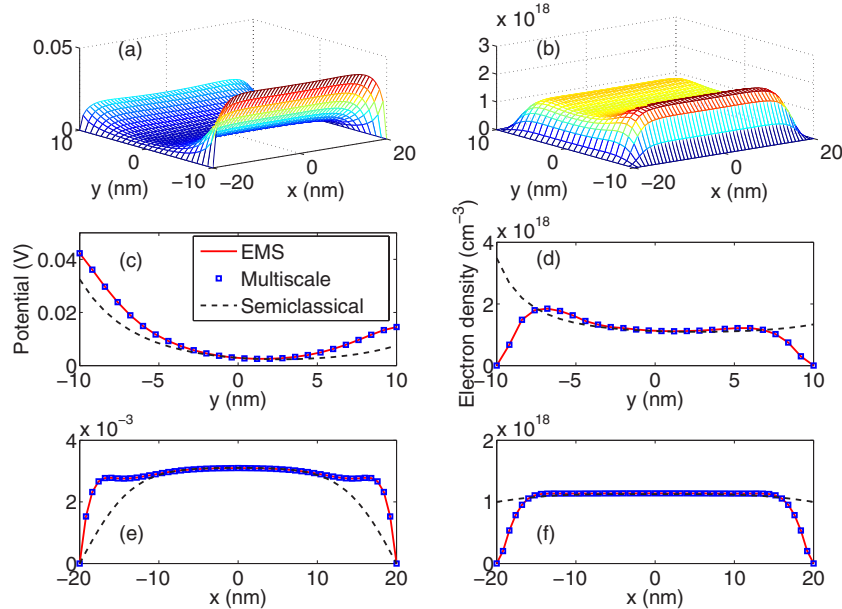


FIG. 7. (Color online) Comparison of the potential and the electron density obtained from the semiclassical, EMS, and multiscale models. Plots (a) and (b) show the potential and the electron density profiles obtained with the multiscale model. Plots (c) and (e) compare the potential computed by the multiscale, EMS, and semiclassical models along the y axis for the $x=0$ cross section and along the x axis for the $y=0$ cross section, respectively. Plots (d) and (f) compare the electron density computed by the multiscale, EMS, and semiclassical models along the y axis for the $x=0$ cross section and along the x axis for the $y=0$ cross section, respectively.

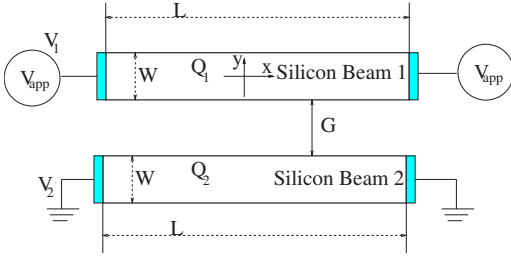


FIG. 8. (Color online) A nanowire system consisting of two fixed-fixed silicon semiconductors.

and 2, respectively, and V_1 and V_2 are the applied voltages on semiconductors 1 and 2, respectively. In this example, the entire system is assumed neutral, i.e., $Q_1 + Q_2 = 0$, and V_2 is fixed to be the ground voltage, i.e., $V_2 = 0$ V. This results in the relation $C_{11} = -C_{12}$. Therefore we only need to compute the mutual capacitance C_{21} to characterize the capacitance of the system. To compute the mutual capacitance C_{21} , we have tested a series of NEMS by choosing $W = 10, 100$, and 1000 nm, and $L = 10W = 10G$. Because the EMS model is computationally very expensive, we use it for only two cases (i.e., for $W = 10$ and 100 nm).

The results for the three cases are shown in Fig. 9. In the case of $W = 10$ nm, the quantum effects are important as shown in Fig. 9(a). The semiclassical model cannot predict the capacitance correctly, as it does not consider the quantum capacitance which cannot be ignored at nanometer scale.²⁹ The result from the classical model, where the equal poten-

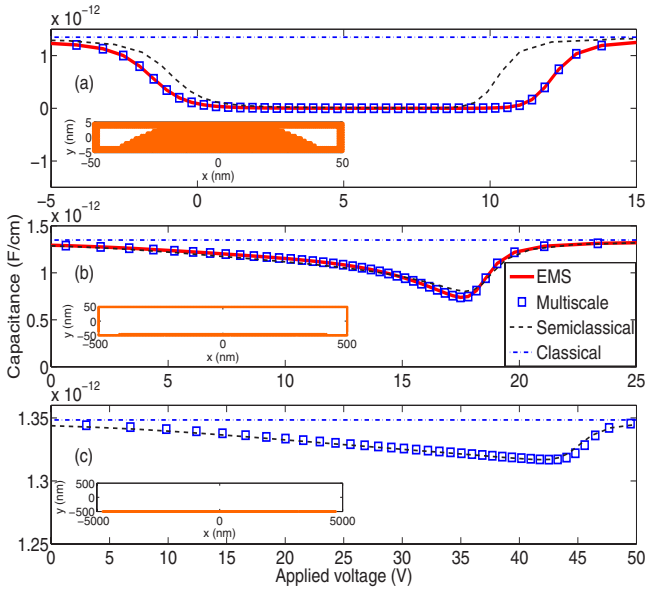


FIG. 9. (Color online) Mutual capacitance C_{12} as a function of applied voltages V_{app} for the two semiconductors for different geometries: (a) $L = 10W = 10G = 100$ nm, (b) $L = 10W = 10G = 1000$ nm, and (c) $L = 10W = 10G = 10$ μ m. The inset in each figure shows the multiscale domain of the upper semiconductor beam when $V_{app} = 10$ V. The semiclassical model is applicable at the sampling Poisson point if $|\phi_q(\mathbf{x})|/\max|\phi| \leq \nu_{tol}$, where ν_{tol} is the given tolerance (a value of 1×10^{-2} is used here). The shaded region indicates the quantum region, whereas the white region indicates the semiclassical region.

tial theory is used, is also shown for comparison and the classical model predicts a constant capacitance as a function of the applied voltage, which is not accurate. The results from the EMS and the multiscale models agree and the multiscale model is about 150 times faster compared to the EMS model. The inset in Fig. 9(a) shows the multiscale domain of the upper semiconductor beam when $V_{app} = 10$ V; because of the strong applied electric field the quantum region is about 70% of the beam. In the case of $W = 100$ nm, as shown in Fig. 9(b), the multiscale model and the semiclassical model give almost the same results, as the quantum capacitance is relatively small compared with the structure capacitance. The inset in Fig. 9(b) shows the multiscale domain of the upper semiconductor beam when $V_{app} = 10$ V. The quantum region is about 6% in this case. The multiscale method is about 1.5 times slower compared to the semiclassical method but more than 2000 times faster than the EMS method. The additional cost of the multiscale method compared to the semiclassical method is due to the small quantum region present in this example. The classical conductor model does not give accurate results in this case as the Debye screening length of the silicon semiconductor is comparable with the size of the semiconductor and this is not accounted for in the classical model. In the case of $W = 1000$ nm, as shown in Fig. 9(c), the results from the semiclassical and multiscale models are almost identical and are very close to the results predicted by the classical model, indicating that at this length scale the classical model is a reasonable approximation to predict the electronic properties. The multiscale domain of the upper semiconductor beam with $V_{app} = 10$ V is also shown in the inset of Fig. 9(c). The quantum region is less than 0.8% and the multiscale method is about 7% slower compared to the semiclassical method. From the results presented in Fig. 9, we can conclude that the multiscale method is an accurate and an efficient tool to compute the electronic properties at all length scales.

C. Heterostructure example

To further explore the effectiveness of the multiscale method, we apply it to a simplified $\text{Al}_x\text{Ga}_{1-x}\text{As}/\text{GaAs}$ heterojunction structure shown in Fig. 10. The $\text{Al}_x\text{Ga}_{1-x}\text{As}$ layers comprise an intrinsic spacer layer followed by an N -type doped $\text{Al}_x\text{Ga}_{1-x}\text{As}$ layer. The substrate of the structure consists of an undoped semi-insulating GaAs layer. A conducting channel in nanoscale is formed in the GaAs layer near the heterojunction interface by electron transfer from the wide band-gap $\text{Al}_x\text{Ga}_{1-x}\text{As}$ layer to the narrow band-gap GaAs layer. The spacer layer acts to separate the conducting channel from the doped layer. The electrons in the conducting channel have a high mobility because the impurity scattering has been strongly reduced by the spatial separation of the electrons and the ionized donors.^{2,3} For the case considered here, we choose $x = 0.4$, the applied voltage to be zero, the doping density N_D of the doped $\text{Al}_x\text{Ga}_{1-x}\text{As}$ layer is 2×10^{18} cm^{-3} , the thickness of the doped $\text{Al}_x\text{Ga}_{1-x}\text{As}$ layer T_1 is 48 nm, the thickness of the undoped $\text{Al}_x\text{Ga}_{1-x}\text{As}$ layer T_2 is 4 nm, the thickness of the GaAs layer T_3 is 100 nm, the length of the top gate L_1 is 32 nm, and the length of the

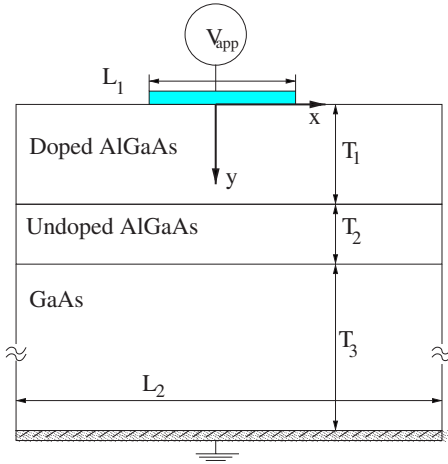


FIG. 10. (Color online) A simplified $\text{Al}_x\text{Ga}_{1-x}\text{As}/\text{GaAs}$ heterostructure.

simulated structure L_2 is 64 nm. Using the “nearsightedness” principle, a sampling radius of 7.5 nm is considered. For simplicity, we neglect the small difference in effective-mass between $\text{Al}_x\text{Ga}_{1-x}\text{As}$ and GaAs, and we also use the same permittivity for both $\text{Al}_x\text{Ga}_{1-x}\text{As}$ and GaAs. The Fermi energy is constant throughout the system in equilibrium and is set to be zero. Thus the conduction band edge at the top gate electrode is fixed to be the value corresponding to the Schottky-barrier height. We choose 1.0 eV for the Schottky-barrier energy in this case which is a reasonable approximation for metal- $\text{Al}_x\text{Ga}_{1-x}$ contact. We fix the down gate to be grounded and ignore the substrate’s Schottky contact. The above assumptions are reasonable for simple simulations and already adopted in Ref. 30.

Next, we perform a self-consistent calculation to find the electron density and conduction band distribution. Note that there is a conduction band discontinuity ΔE_c at the $\text{Al}_x\text{Ga}_{1-x}\text{As}/\text{GaAs}$ interface. The quantum-mechanical and semiclassical regions are again identified by the quantum potential criterion and the multiscale method seamlessly combines the two regions. The Schottky-barrier, conduction band discontinuity, and physical boundary barrier form quantum wells which confine the electrons and induce significant

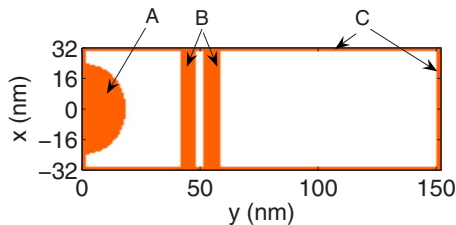


FIG. 11. (Color online) Illustration of the multiscale domain for the heterojunction structure for the case shown in Fig. 10. The semiclassical model is applicable at the sampling Poisson point if $|\phi_q(x)|/\max|\phi| \leq \nu_{\text{tol}}$, where ν_{tol} is the given tolerance (a value of 1×10^{-2} is used here). The shaded region indicates the quantum region, whereas the white region indicates the semiclassical region. The quantum regions A, B, and C are formed by the electric field due to the Schottky barrier, conduction band discontinuity, and physical boundary barrier, respectively.

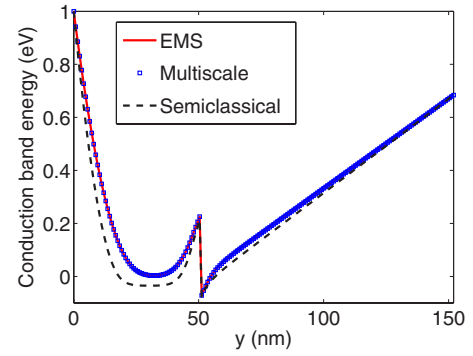


FIG. 12. (Color online) Comparison of the conduction band energy predicted by the EMS, multiscale, and semiclassical models for the $\text{Al}_x\text{Ga}_{1-x}\text{As}/\text{GaAs}$ based quantum heterostructure along the y axis for the $x=0$ cross section.

variation in the charge density along the y direction. By using the quantum potential criterion [Eq. (34)], three quantum regions are identified as shown in Fig. 11. The first quantum region (the semicircularlike region A in Fig. 11) is formed by the electric field because of the Schottky barrier of the metal-semiconductor contact. The second quantum region (region B) is formed by the built-in electric field due to the conduction band discontinuity at the $\text{Al}_x\text{Ga}_{1-x}\text{As}/\text{GaAs}$ interface region. The last quantum region (region C) is formed by the physical boundary barrier which surrounds the entire semiconductor structure. About 24% of the semiconductor region is quantum mechanical in this case.

Since the conduction energy and electron density near the heterojunction are the interesting features, their distribution along the y axis for the $x=0$ cross section obtained by the EMS, multiscale, and semiclassical models is shown in Figs. 12 and 13, respectively. From these results, we conclude that the semiclassical model fails to predict the electronic properties, whereas the multiscale model gives the same results as the EMS model, but the multiscale method is about 1000 times faster compared to the solution of the EMS model.

IV. CONCLUSIONS

A multiscale model combining semiclassical and effective-mass Schrödinger theories has been presented in

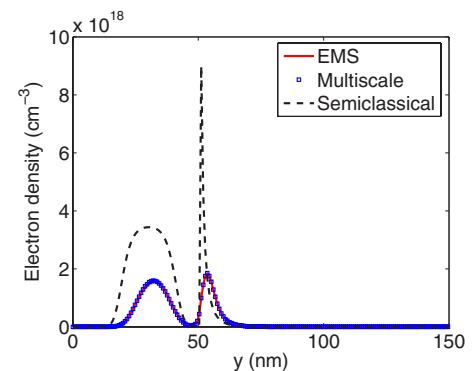


FIG. 13. (Color online) Comparison of the electron density predicted by the EMS, multiscale, and semiclassical models for the $\text{Al}_x\text{Ga}_{1-x}\text{As}/\text{GaAs}$ based quantum heterostructure along the y axis for the $x=0$ cross section.

this paper for electrostatic analysis of semiconductor nanostructures. A quantum potential criterion is used to identify semiclassical and quantum-mechanical regions. In the regions, where the quantum effects are significant, the electron densities are computed by considering sampling regions and the local density of states. The multiscale method has been shown to be accurate by comparing results with the EMS theory. When the quantum regions are significant, the multiscale method has been shown to be several orders of magnitude faster compared to the direct solution of the effective-mass Schrödinger equation. When the quantum regions are

insignificant, the multiscale method approaches the efficiency of the semiclassical method. We have also shown that the multiscale method can be used to delineate the quantum and semiclassical regions for problems in NEMS and nano-electronics.

ACKNOWLEDGMENTS

This work is supported by the National Science Foundation under Grants No. 0228390 and No. 0601479, by DARPA/MTO, and SRC.

*Corresponding author. aluru@uiuc.edu; <http://www.uiuc.edu/~aluru>

¹H. G. Craighead, *Science* **290**, 1532 (2000).

²C. Weisbuch and B. Vinter, *Quantum Semiconductor Structures: Fundamentals and Applications* (Academic Press, London, 1991).

³K. F. Brennan, *Introduction to Semiconductor Devices: For Computing and Telecommunications Applications* (Cambridge University Press, Cambridge, UK, 2005).

⁴Y. T. Yang, K. L. Ekinici, X. M. H. Huang, L. M. Schiavone, M. L. Roukes, C. A. Zorman, and M. Mehregany, *Appl. Phys. Lett.* **78**, 162 (2001).

⁵L. Pescini, H. Lorenz, and R. H. Blick, *Appl. Phys. Lett.* **82**, 352 (2003).

⁶N. R. Aluru and J. White, *Sens. Actuators, A* **58**, 1 (1997).

⁷G. Li and N. R. Aluru, *IEEE Trans. Comput.-Aided Des.* **22**, 1228 (2003).

⁸Z. Tang, Y. Xu, G. Li, and N. R. Aluru, *J. Appl. Phys.* **97**, 114304 (2005).

⁹D. K. Ferry, *Superlattices Microstruct.* **27**, 61 (2000).

¹⁰H. L. Grubin, J. P. Kreskovsky, T. R. Govindan, and D. K. Ferry, *Semicond. Sci. Technol.* **9**, 855 (1994).

¹¹I. Knezevic, D. Vasileska, and D. K. Ferry, *IEEE Trans. Electron Devices* **49**, 1019 (2002).

¹²A. Asenov, J. R. Watling, A. R. Brown, and D. K. Ferry, *J. Comput. Electron.* **1**, 503 (2002).

¹³D. K. Ferry, S. Ramey, L. Shifren, and R. Akis, *J. Comput. Electron.* **1**, 59 (2002).

¹⁴B. Winstead, H. Tsuchiya, and U. Ravaioli, *J. Comput. Electron.*

1, 201 (2002).

¹⁵Y. Li, T. Tang, and X. Wang, *IEEE Trans. Nanotechnol.* **1**, 238 (2002).

¹⁶S. S. Ahmed, C. Ringhofer, and D. Vasileska, *IEEE Trans. Nanotechnol.* **4**, 465 (2005).

¹⁷R. F. Pierret, *Semiconductor Device Fundamentals* (Addison-Wesley, Reading, MA, 1996).

¹⁸G. Li and N. R. Aluru, *J. Appl. Phys.* **96**, 2221 (2004).

¹⁹J. H. Kane, *Boundary Element Analysis in Engineering Continuum Mechanics* (Prentice-Hall, Englewood Cliffs, NJ, 1994).

²⁰J. D. Jackson, *Classical Electrodynamics*, 3rd ed. (Wiley, New York, 1999).

²¹M. T. Heath, *Scientific Computing: An Introductory Survey*, 2nd ed. (McGraw-Hill, New York, 2002).

²²E. N. Economou, *Green's Functions in Quantum Physics* (Springer-Verlag, Berlin, 1983).

²³C. Lanczos, *J. Res. Natl. Bur. Stand.* **45**, 255 (1950).

²⁴A. Jennings and J. J. McKeown, *Matrix Computation* (Wiley, New York, 1992).

²⁵R. Haydock, *Recursion Method and Its Applications* (Springer-Verlag, Berlin, 1985).

²⁶K. Hess, *Advanced Theory of Semiconductor Devices* (Prentice-Hall, Englewood Cliffs, NJ, 1988).

²⁷W. Kohn, *Phys. Rev. Lett.* **76**, 3168 (1996).

²⁸E. Prodan and W. Kohn, *Proc. Natl. Acad. Sci. U.S.A.* **102**, 11635 (2005).

²⁹S. Datta, *Quantum Transport: Atom to Transistor* (Cambridge University Press, New York, 2005).

³⁰B. Vinter, *Appl. Phys. Lett.* **44**, 307 (1984).